

Validation of unstructured-mesh LES of the trailing-edge flow and noise of a Controlled-Diffusion airfoil

By S. Moreau[†], D. Neal[‡], Y. Khalighi, M. Wang[¶], AND G. Iaccarino

Large-Eddy Simulations (LES) of flow over a low-speed airfoil is performed using an unstructured-mesh flow solver with an efficient mesh-refinement strategy. Results from three different grids are compared against a reference structured-mesh solution, which was previously shown to provide a reasonably accurate trailing-edge flow for noise predictions. These simulations are compared with detailed pressure and velocity measurements made using flush-mounted remote microphone probes and hot-wire anemometry, respectively. The observed discrepancies are shown to have a small impact on the acoustic predictions, which compare favorably with the anechoic wind tunnel measurements. The effects of finite chord length and exact Green's function on the noise levels are also assessed.

1. Introduction

Trailing-edge noise or broadband self-noise, caused by the scattering of boundary-layer vortical disturbances into acoustic waves, occurs at the trailing edge of a lift-generating device, and is a major source of noise generated by fans (Sharland 1964; Wright 1976; Fukano *et al.* 1977; Caro & Moreau 2000), wind turbines (Glegg *et al.* 1987; Hubbard & Shepherd 1991; Parchen *et al.* 1999), and other high-lift devices (Pérennès & Roger 1998; Singer *et al.* 2000). These noise levels can be reduced by properly identifying the sources of self-noise, and subsequently modifying design parameters that affect these noise sources. The large computational costs associated with the unsteady turbulent flow simulations have limited previous studies to simplified devices such as airfoils. A first LES of the flow over the Valeo Controlled-Diffusion (CD) airfoil by Wang *et al.* (2004) using a structured mesh showed that a large grid with 5.1 million nodes was needed to yield stable and accurate flow solutions. Subsequent attempts to reduce the computational costs included the use of non-boundary conforming methods such as the Lattice Boltzmann method and Immersed Boundary method (Moreau *et al.* 2004), as well as hybrid solution methods such Detached Eddy Simulations (Moreau *et al.* 2005). These techniques yielded less accurate mean wall-pressure distributions (larger laminar recirculation bubble near the leading edge and possibly turbulent flow separation near the trailing edge) and frequency spectra near the trailing edge than those obtained by Wang *et al.* (2004).

The alternative approach taken here involves LES with unstructured grid topologies, which is known to significantly reduce the number of nodes and the amount of time required for grid generation. Several different strategies for the grid coarsening are explored with the aim of consequently moving to a realistic fan blade as shown in Moreau

[†] Valeo Thermal Systems 78321 La Verrière, France

[‡] Michigan State University, East Lansing, MI 48824

[¶] University of Notre Dame, Notre Dame, IN 46556

et al. (2006b). The validation of these concepts is performed by comparing the LES results obtained with the unstructured flow solver CDP with both the previous results of Wang *et al.* (2004) and the experimental data collected over several years at two different test facilities. The final section assesses the impact of these unstructured grid topologies on the trailing-edge noise predictions. Two different approaches have been explored to model the far field acoustic pressure: the extended Amiet's theory by Roger & Moreau (2005) based on the diffraction of pressure fluctuations near the trailing edge by a flat plate of finite chord, and an integral-form solution to the Lighthill equation using either an approximate hard-wall Green's function for a semi-infinite flat plate (Ffowcs Williams & Hall, 1970) or the exact numerical Green's function of the airfoil. The former relies on the wall-pressure statistics near the trailing edge and the latter on the velocity statistics in the near wake. This region of the flow is therefore the main focus of the aerodynamic validation shown in the next sections.

2. Experiments using hot-wire anemometry and unsteady pressure measurements

2.1. Experimental setup

The experimental data were collected at two separate facilities. The large anechoic wind tunnel of the Ecole Centrale de Lyon (ECL) was initially used for the wall-pressure measurements and some of the hot-wire measurements (Moreau *et al.*, 2003). The 0.61 m^2 tunnel of the Turbulent Shear Flow Laboratory (TSFL) at Michigan State University (MSU) was then used for additional hot-wire measurements. The MSU 0.61 m^2 tunnel was modified to closely match the configuration found at the ECL. Inlet velocity surveys were conducted to confirm that there was a consistent upstream condition for the CD airfoil in each case. The airfoil mock-up has a 13.4 cm constant chord length (c) and a 0.3 m span (L). It is held between two horizontal side plates fixed to the nozzle of the open-jet for each of the two wind tunnels. These plates are 25 cm ($\approx 1.85 c$) apart and the width of the rectangular jet is 50 cm ($\approx 3.7 c$). All of the tests were run with a speed $U_\infty = 16\text{ m/s}$, which corresponds to a Reynolds-number based on the airfoil chord length $Re_c = 1.6 \times 10^5$. An angle of attack α_g of 8° was kept consistently for all the tests.

The CD airfoil mock-up is equipped at midspan with 21 flush-mounted remote microphone probes (RMP) (Pérennès & Roger 1998). The RMPs measure both the mean and fluctuating pressure within a frequency range of 20 Hz–25 kHz. Figure 1 (left) shows the layout of the streamwise RMPs at the midspan plane of the CD airfoil. Three additional RMPs in the spanwise direction near the trailing edge allow measuring spanwise coherence lengths. Details of the wall-pressure measurements in this configuration can be found in Moreau & Roger (2005).

2.2. Hot-wire measurements

Hot-wire measurements were collected in the regions shown in Fig. 1 (right) to provide more detailed information on the mean and root-mean-square (rms) flow quantities and velocity spectra. For certain regions of the flow, single-normal (SN) probes were used, given their small active sensor length and relative ease of use. Initial RANS simulations indicated that certain regions of the mean flow and bounding shear layers were strongly influenced by the CD airfoil, resulting in a flow that had significant two-dimensional features. This observation necessitated the use of X-probes for resolving two components of the flow. Both the SN-probes and X-probes were designed and fabricated by the MSU-

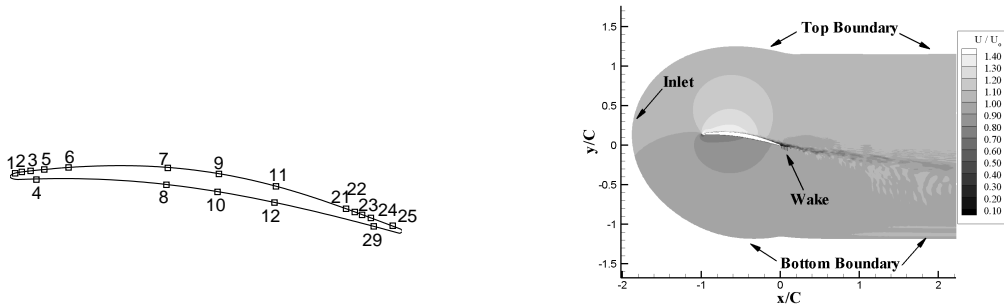


FIGURE 1. Data locations. Left: RMP locations on the CD airfoil. Right: Locations of velocity surveys.

TSFL. The design of this probe follows on the recommendations of Strohl & Comte-Bellot (1973); further details can be found in Moreau *et al.* (2006a). These probes were used with a standard TSI IFA-100 anemometer at ECL and a similar TSI IFA-300 at MSU. The data were sampled at 30 kHz for durations between 30–60 s, depending on the time needed for converged statistics. The frequency response of all of the probes used was found to be between 30–50 kHz.

The hot-wire probes have been calibrated in a separate calibration tunnel designed by the MSU-TSFL, for speeds ranging from 2–20 m/s. Further details of this calibration facility and procedures can be found in Moreau *et al.* (2006). The X-probe has the requirement that the incoming velocities fall within the angle range $|\gamma| > \pm 36^\circ$. The probe orientations for the X-probe were established by analyzing the results of the LES and RANS calculations described in Wang *et al.* (2004). Further details of this analysis can be found in Moreau *et al.* (2006). The ambient temperature of the flow in the vicinity of the hot-wire was measured using a thermocouple. It was found to drift by as much as 8° over the data set interval (pre-to-post-calibration time period). These effects were compensated using the so-called “linear temperature compensation” described by Abdel-Rahman *et al.* (1987).

The power spectral density of these processed hot-wire results were obtained by dividing the total time series into smaller records of 1024 points. This length was determined to be sufficiently long to capture the large scales, yet short enough to have enough records for smooth spectra. These time records were transformed into the Fourier domain using standard Fast Fourier Transform (FFT) algorithms with a Hanning window. Calculating the spectra for the X-probe data was more complicated since there are isolated regions in which the acceptance angles, γ , exceeded the calibration range ($|\gamma| > \pm 36^\circ$). These points were excluded from the record. A searching algorithm was used to find all the available records of the chosen length (1024). These available records were continuous strings of data of a given length that occurred between the sporadic bad points in the X-probe time series. The uncertainty in the spectral levels is much less than a decibel over the entire frequency range.

3. Large-Eddy Simulations for the CD airfoil

3.1. Flow solvers

The LES is based on the spatially filtered, incompressible Navier-Stokes equations with the dynamic subgrid scale model (Germano *et al.* 1991; Lilly 1992). These are solved using energy-conserving non-dissipative central difference schemes for spatial discretizations and the fractional step method for time advancement (Kim & Moin 1985). This approach yields the hybrid finite difference/spectral code used by Wang & Moin (2000) for structured grid topologies and the control-volume solver CDP developed by Mahesh *et al.* (2004) for hybrid unstructured grids. Further details on the numerical schemes can be found in Wang *et al.* (2004) for the structured mesh code and in Ham & Iaccarino (2004) for the unstructured solver. The present LES use the node-based version CDP_IF2.

3.2. Numerical setup and boundary conditions

The first LES of the CD airfoil performed by Wang *et al.* (2004) closely reproduced the experimental conditions found in the ECL large anechoic wind tunnel. As shown by Moreau *et al.* (2003), a two-dimensional (2-D) Reynolds-Averaged Navier-Stokes (RANS) simulation of the complete open-jet wind tunnel configuration is required to capture the strong interaction between the jet and the CD airfoil and its impact on the airfoil load.

The RANS simulation provides velocity boundary conditions for the smaller LES domain shown in Fig. 1 (right), which is embedded between the two boundary shear layers of the jet. This method follows a similar strategy used in the trailing-edge flow simulation of Wang & Moin (2000). Yet, the lower Reynolds number Re_c and the relatively large jet-width to chord ratio in the present case allows a computational domain around the full airfoil: 4 c in the streamwise (x) direction and 2.5 c in the crosswise (y) direction. A much larger width (0.1 c) is also used in the spanwise (z) direction. The LES use a no-slip boundary condition on the airfoil surface, a convective outflow boundary condition at the exit plane, and the steady RANS velocity (U and V) along the upper and lower boundaries. Periodic boundary conditions are applied in the spanwise direction.

3.3. Grid topologies

A single block-structured C-mesh, shown in Fig. 2 (left), with $960 \times 84 \times 64$ cells is used in the reference LES by Wang *et al.* (2004). Smooth-grid distribution and orthogonality at the wall were found to be critical at the leading edge to properly capture the laminar-boundary layer on the pressure side and the transitional- and turbulent-boundary layer on the suction side with the correct laminar separation bubble size. Moreover, the grid-stretching ratio needs to be limited in the streamwise and cross-flow directions to ensure numerical stability. Simulations performed on this grid with CDP are termed CDP-A.

In addition to this structured mesh, two new unstructured meshes have been designed. The first case involves taking the structured mesh in the x - y plane and performing a grid coarsening in the spanwise direction only. The grid is coarsened in proportion to the distance from the airfoil. To prevent the poor mesh quality triggered by hanging nodes, a smooth transition is implemented by inserting one transitional layer of pyramids or wedges between two consecutive levels of hexahedra grid refinement by a factor of two. This transitional layer can be seen in Fig. 3 where a hexahedra is cut into two wedges. The overall number of nodes is then reduced from 5.1 million to 1.5 million. The second case simply generalizes the mesh expansion technique to all directions. This final unstructured mesh has six levels of grid coarsening in the x - y plane. The near-wall region has the same resolution as the two previous configurations and a boundary-layer type mesh is kept

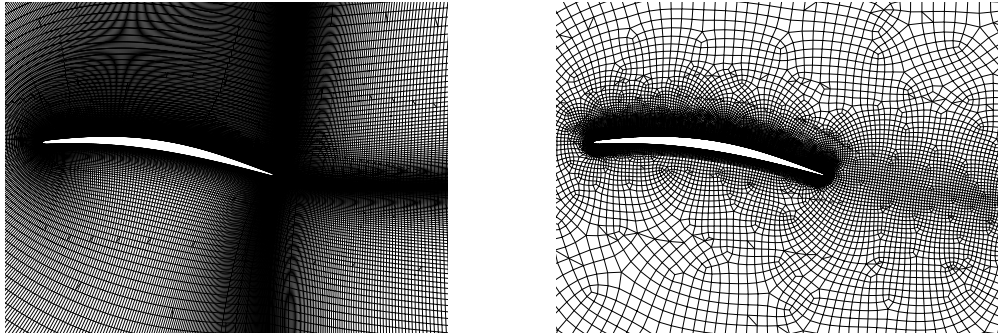


FIGURE 2. Mesh configurations in x - y plane. Left: CDP-A and CDP-B. Right: CDP-C.

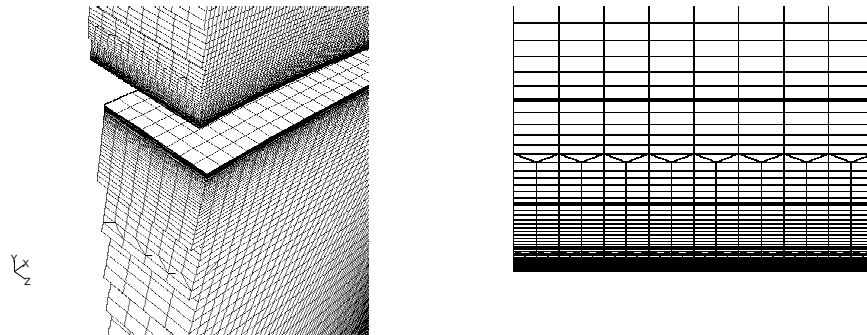


FIGURE 3. Grid expansion technique. Left: Cut of the 3-D unstructured mesh through the airfoil. Right: Close-up view of the grid expansion in the vicinity of the wall.

close to the walls. Points are also clustered around the wake that was captured by the previous RANS simulations. Elsewhere the grid was aggressively coarsened to yield a final mesh whose 2-D cut is shown in Fig. 2 (right). The final 3-D mesh has only 1.1 million cells. Simulations performed on these new unstructured grids with CDP are labeled CDP-B and CDP-C, respectively. The number of cells and the type of element for all grids are summarized in Fig 4 (left). It shows that the present expansion scheme can yield considerable savings in computational costs.

4. Aerodynamic results

4.1. Mean pressure coefficient ($-C_p$) and pressure spectra

The mean and fluctuating wall pressure were analyzed for each of the LES runs and compared with the RMPs measurements by Moreau & Roger (2005). The mean pressure on the surface, characterized by the pressure coefficient $-C_p$, is shown in the right-hand side of Fig. 4. These results show that the two expanded LES cases are in reasonably good agreement with the results of Wang *et al.* (2004). All LES capture the boundary-layer transition on the suction side, which is triggered by an unsteady laminar separation near the leading edge. The one discrepancy appears to be on the suction side around

	CDP-A	CDP-B	CDP-C
3-D mesh	5.1 M	1.5 M	1.1 M
2-D mesh	80.8 K	80.8 K	38.8 K
Hex	100%	91.5%	91.6%
Prism	0%	7.0%	7.7%
Pyramid	0%	1.3%	0.6%
Tet	0%	0.2%	0.1%

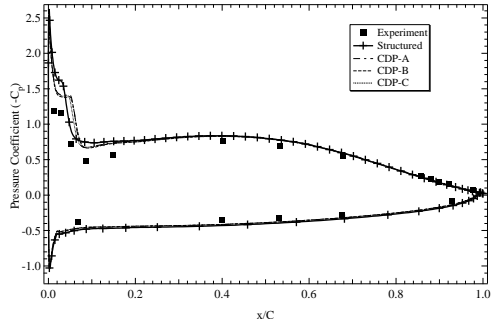


FIGURE 4. Left: The mesh features of the three different structured and unstructured grid configurations. Right: Mean wall-pressure coefficient $-C_p$ along the airfoil.

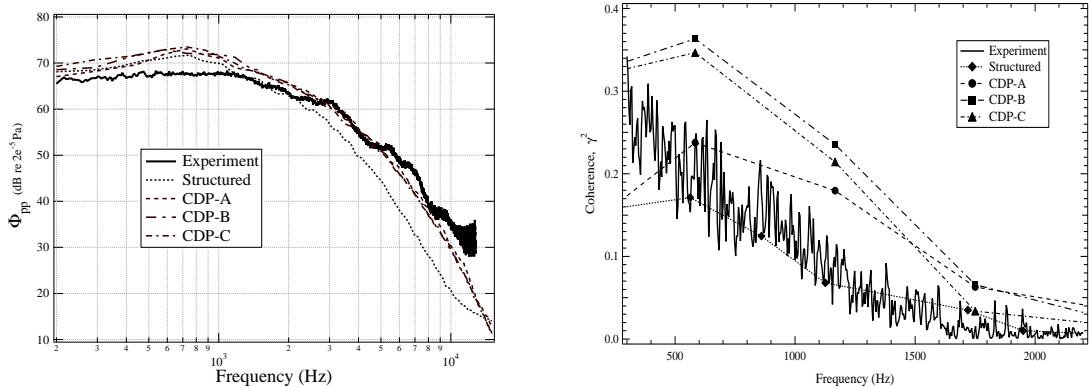


FIGURE 5. Pressure fluctuation data. Left: Power spectral density of wall pressure near the trailing edge ($x/C = -0.02$ on suction side). Right: Spanwise coherence at the same location for a spanwise separation $\Delta z/c = 0.02$.

$x/c \approx 0.1$, where all the unstructured LES cases (CDP-A, B and C) slightly over-predict the recirculation bubble size (5% c) compared to the previous structured LES (3.7% c). Yet, as in the previous simulation with STAR-CD by Moreau *et al.* (2005), which also had too large a laminar flow separation (11.2% c), these runs start capturing the experimental positive pressure gradient at 15% of chord. Therefore both the extent of the laminar separation region and the consequent positive pressure gradient are more dependent on the LES code and mostly on its subgrid-scale model implementation than on the grid itself provided it is fine and sufficiently regular near the wall.

The wall-pressure spectra near the trailing edge are shown in the left plot of Fig. 5. The LES results on the coarsened grids (CDP-B and CDP-C) are very similar to the LES on the reference fine grid of Wang *et al.* (2004) (CDP-A), particularly for $f \geq 1500$ Hz. All CDP results also show better agreement with the experimental data over the same frequency range than those obtained by Wang *et al.* (2004), which tail off more quickly with frequency. For lower frequencies ($f \leq 1500$ Hz), all LES runs yield higher PSD levels than the experiment. Yet both the structured and CDP-A runs on the same finer grid show similar closer levels. Figure 5 (right) shows the spanwise coherence plots as a function of frequency for a spanwise sensor separation $\Delta z/c = 0.02$. All CDP results over-predict the coherence. A comparison between CDP-A and the reference LES suggests that the current results do not have a long enough time record for proper convergence

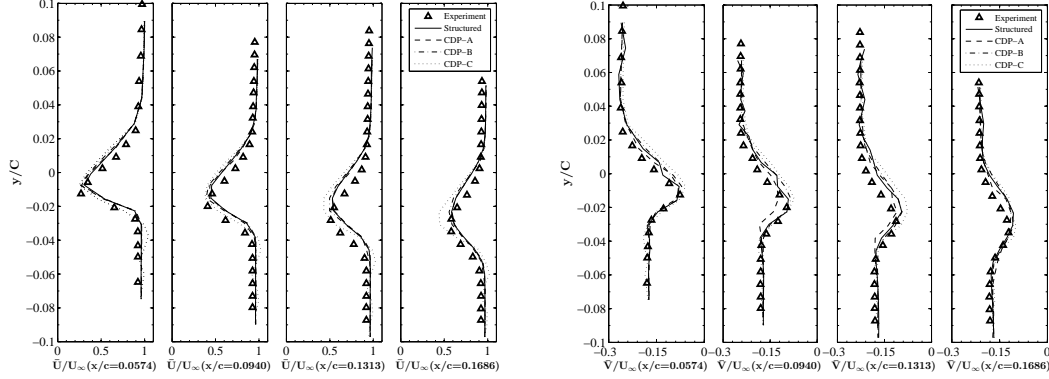


FIGURE 6. Wake velocity data. Left: Normalized mean velocity \bar{U}/U_∞ at four x/c locations.
Right: Normalized mean velocity \bar{V}/U_∞ at four x/c locations.

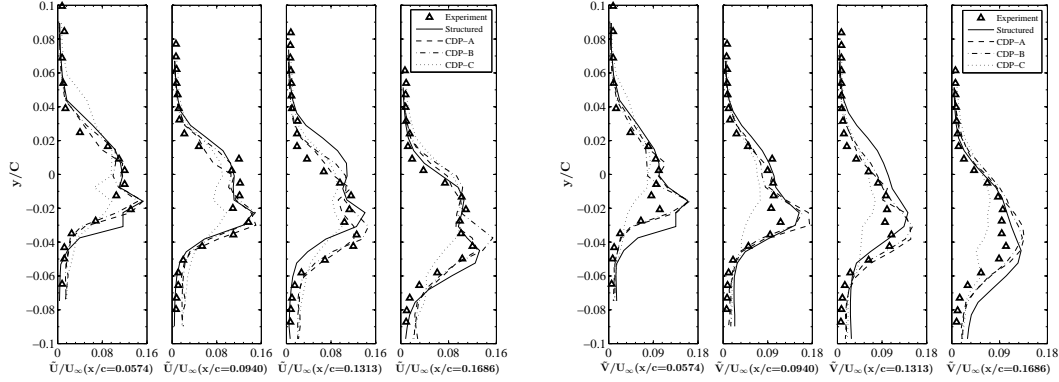


FIGURE 7. Wake velocity data. Left: Normalized rms velocity fluctuations \tilde{U}/U_∞ at four x/c locations. Right: Normalized rms velocity fluctuations \tilde{V}/U_∞ at four x/c locations.

and proper sampling at lower frequencies. A comparison among the CDP results also suggests that the spanwise grid stretching in the CDP-B and C runs yields worse results.

4.2. Velocity statistics in the wake

Velocity data were extracted for each of the LES runs, at locations that matched those of the hot-wire probes in the experiment of Moreau *et al.* (2006a). A total of 8 stations in the near wake were measured experimentally, ranging from $x/c = 0.0574$ to $x/c = 1.0133$. Figure 6 shows the mean velocity components (\bar{U} and \bar{V} respectively) at four different measurement stations from $x/c = 0.0574$ to $x/c = 0.1686$. For the first station, each of the CDP runs and also the velocity results of Wang *et al.* (2004), have very similar shapes, with the wake deficits very close to those of the experiment. There is approximately a 3–4% lower velocity in the experiment at the locations just outside of the wake. Similarly, there is a higher \bar{V} velocity for the experiment at these same locations. The overall velocity magnitude measured in the experiment is lower than for each of the LES. The results of CDP-C show an oscillation on the pressure side of the airfoil for both \bar{U} and \bar{V} . This appears to be caused by spurious energy being added into the mean velocity

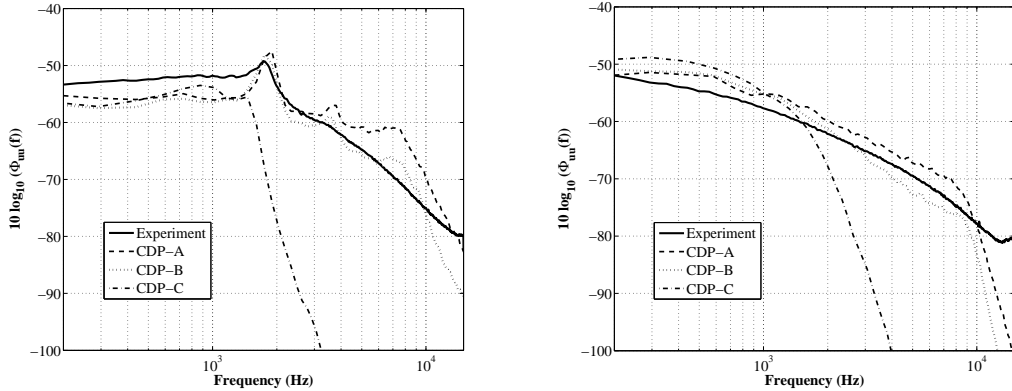


FIGURE 8. Wake energy spectra of the streamwise velocity. Left: Pressure Side at $(x,y)=(0.057,-0.023)$. Right: Suction Side at $(x,y)=(0.057,0.015)$.

components; a result of either the initial unstructured grid or the grid-coarsening method. The next two measurement stations show that the wake deficit is poorly predicted by CDP-C. At the last location shown, $x/c = 0.1686$, there is a 20% difference between the experiment and CDP-C at the peak wake velocity deficit. The grid for CDP-C is under-predicting dissipation in the wake. This location is sufficiently far from the airfoil surface, and the number of spanwise nodes has decreased by a factor of 4, from 64 to 16.

The rms of velocity fluctuations (\tilde{U} and \tilde{V} respectively) are shown in Fig. 7. Each of the LES runs has a profile that is qualitatively similar to that of the experiment. The striking feature is that the location of the peak turbulence intensity (the location of the highest shear in the wake) is within a length $\Delta y/c \leq 0.04$ of the experiments. The overall peak turbulence intensity levels are lowest for CDP-C, although it closely predicts the qualitative shape of both \tilde{U} and \tilde{V} at the first three stations. However, by the farthest downstream location, CDP-C is even qualitatively different and it can no longer predict the location of the peak turbulence intensity. These lower levels for CDP-C can be attributed both to the lower resolution of the mesh in the spanwise direction (as compared with CDP-A), along with the different 2-D mesh (as compared with both CDP-A and CDP-B). The observed differences are likely caused by the back-scattering of unresolved energy, which has a dissipative effect on the relative turbulence levels.

4.3. Wake spectra

The velocity energy spectra in the wake region were measured experimentally for frequencies up to 15 kHz. For the three CDP-LES cases, a time series of nominally 17,000 points was separately saved from the simulations. These data are used to calculate the power spectral density at the 153 different downstream locations in the wake, which are located at the same x/c as those described in Section 4.2. Figure 8, which plots the streamwise velocity energy spectra at $x/c = 0.057$ and two cross-flow locations $y/c = -0.023$ (left) and $y/c = 0.015$ (right), shows that there is a 2–3 dB variation at lower frequencies ($f \leq 2000$ Hz), but good qualitative agreement with the experiments for CDP A-C. At $f \approx 2000$ Hz, a shedding frequency is measured on the lower side of the wake. This feature is captured by CDP A and B, but not C, which rolls off prematurely. This suggests that the spanwise grid spacing at this point is larger than the coherence of the U -velocity in the spanwise direction. As a result, it destroyed the small-scale eddies and

thus damped out the energy in the other directions as well. CDP A and B over-predict the pressure-side energy shown in the left plot of Fig. 8. Specifically, they show a PSD level that is 5–10 dB higher between 6–10 kHz in this region.

5. Acoustic predictions

5.1. Overview of methods

In Amiet's theory, the trailing-edge noise is derived by iteratively solving scattering problems at the airfoil edges. The system of partial differential equations that arise at each iteration in this multiple scattering problem is solved by the standard Schwarzschild's solution. The main trailing-edge scattering is first determined assuming that the airfoil surface extends toward infinity in the upstream direction. Amiet (1976) reduced the formulation to this first evaluation and calculated the radiated sound field by integrating the induced surface sources on the actual chord length, c and the mock-up span, L , assuming convection of frozen turbulent boundary layer eddies past the trailing edge. This provides a first evaluation of the radiation integral I , say $I \simeq I_1$. A leading-edge correction fully taking into account the finite chord length (second iteration and correction I_2 to I) has been derived recently by Roger & Moreau (2004, 2005). The predicted sound field in the midspan plane at a given observer location $\vec{x} = (x_1, x_2, 0) = (R, \theta, z = 0)$ and for a given radian frequency ω (or wavenumber k) then reads

$$S_{pp}(\vec{x}, \omega) = p_a(\vec{x}, \omega) p_a^*(\vec{x}, \omega) = \left(\frac{\sin \theta}{2\pi R} \right)^2 (k c)^2 \frac{L}{2} |I|^2 \Phi_{pp}(\omega) l_y(\omega) \quad (5.1)$$

where Φ_{pp} is the wall-pressure power spectral density and l_y the spanwise correlation length near the trailing edge. The radiation integral $I = I_1 + I_2$ involving both the free stream velocity U_∞ and the convection speed as parameters are given by Roger & Moreau (2005).

In Ffowcs Williams-Hall's theory, a half-plane hard-wall Green's function, whose normal derivative vanishes on the surface, is used to provide a correct integral solution to the Lighthill equation using incompressible source field data. The far field acoustic pressure at a given observer location \vec{x} and for a given radian frequency ω can be written in the form

$$\begin{aligned} p_a^\infty(\vec{x}, \omega) &= \frac{2e^{-i\pi/4}}{\pi^{1/2}} k^2 \sin\left(\frac{\theta}{2}\right) \int_V \frac{e^{ikR}}{4\pi R} \frac{(\sin\phi)^{1/2}}{(2kr_0)^{3/2}} \\ &\times \left\{ \rho_0 \left(\widehat{U_\theta^2} - \widehat{U_r^2} \right) \sin\left(\frac{\theta_0}{2}\right) - 2\rho_0 \widehat{U_r U_\theta} \cos\left(\frac{\theta_0}{2}\right) \right\} d^3\vec{y} \end{aligned} \quad (5.2)$$

where the caret denotes temporal Fourier transform and V is the integration volume around the airfoil trailing edge. The velocity components U_r and U_θ are defined in the cylindrical-polar coordinate system around the trailing edge. The vector $\vec{y}(r_0, \theta_0, z_0)$ represents the source-field points with $R = |\vec{x} - \vec{y}|$ and $\sin\phi = r/[r^2 + (z - z_0)^2]^{1/2}$. As shown by Wang & Moin (2000), a further simplification to Eq. 5.2 can be made if the spanwise extent of the source-field is acoustically compact, which is the case for the source-region contained within the computational domain. Equation 5.2 can then be approximated by

$$p_a^\infty(\vec{x}, \omega) = \frac{e^{i(k|\vec{x}| - \pi/4)}}{2^{5/2} \pi^{3/2} |\vec{x}|} (k \sin\phi)^{1/2} \sin\left(\frac{\theta}{2}\right) \widehat{S}(\omega) \quad (5.3)$$

with

$$S(t) = \int_V \frac{\rho_0}{r_0^{\frac{3}{2}}} \left\{ (U_\theta^2 - U_r^2) \sin\left(\frac{\theta_0}{2}\right) - 2U_r U_\theta \cos\left(\frac{\theta_0}{2}\right) \right\} d^3\vec{y} \quad (5.4)$$

which only involves a single compact source term $S(t)$ easily evaluated during the LES. It should be noted that Eq. 5.3 is strictly valid only when the acoustic wavelength λ is much longer than the thickness of the airfoil h near the trailing edge, but much shorter than the chord ($h \ll \lambda \ll c$). One improvement can be made to Eq. 5.3 by considering the Green's function for a flat plate of finite chord length that has been recently derived by Howe (2001). Similarly to what was found by Gershfeld (2004) for the leading-edge noise, a simple factor of proportionality is derived between the acoustic pressure for a semi-infinite plane $p_a^\infty(\vec{x}, \omega)$ and the one for a finite chord $p_a(\vec{x}, \omega)$. The far field acoustic pressure then reads at midspan and above the airfoil

$$p_a(\vec{x}, \omega) = 2\mathcal{F}\left(\sqrt{\frac{2kc}{\pi}}\right) \frac{\left(\frac{e^{ikc}}{\sqrt{2\pi kc}} - e^{-i\pi/4}\right)}{\left(e^{-ikc} + \frac{e^{ikc}}{2\pi ikc}\right)} p_a^\infty(\vec{x}, \omega) \quad (5.5)$$

with \mathcal{F} the Fresnel integral auxiliary function.

Finally, a more accurate solution for the acoustic pressure can be obtained by removing all the flat plate assumptions and computing the exact Green's function of the cambered airfoil \widehat{G} instead. For a given angular frequency, \widehat{G} is the solution of the Helmholtz equation with Neumann boundary conditions on the airfoil and Sommerfeld far field conditions away from it. A Boundary Element Method has been implemented to solve this problem. The far field acoustic pressure is then simply computed from

$$p_a(\vec{x}, \omega) = \int_V \frac{\partial^2 \widehat{G}(\vec{x}, \vec{y}, \omega)}{\partial y_i \partial y_j} \widehat{T}_{ij}(\vec{y}) d^3\vec{y} \quad (5.6)$$

where \widehat{T}_{ij} is averaged in the spanwise direction, as the zeroth mode of the Lighthill stress tensor is shown to be the dominant contribution to the far field noise.

5.2. Results

To compute the source-terms in Eqs. 5.3 and 5.4 or the full Lighthill's tensor \widehat{T}_{ij} in Eq. 5.6, the velocity components U_i on the entire computational grid were sampled at every 10 time steps during the source-field reference LES and only every 20 time steps for the CDP LES. The sampling resolution $t_s U_1/h \approx 0.029$ for the structured LES and $t_s U_1/h \approx 0.004$ for the CDP LES. The total record of $N = 1152$ time samples, covering a period $T_s U/h \approx 33.47$, is divided into eight segments with a 50% overlap in the structured LES. The total record of $N = 832$ time samples, covering a period $T_s U/h \approx 3.32$, is divided into thirteen segments with a 50% overlap in the CDP LES.

Figure 9 (left) first compares the prediction of Ffowcs Williams-Hall's theory using the reference LES data in Eqs. 5.3 and 5.4, with the ECL measurement in the midspan plane above the airfoil ($\theta = 90^\circ$) at a distance $R = 2$ m. A very favorable agreement is reached over the entire measured frequency range. The effect of the finite chord on the computed noise spectrum is also evidenced. Similarly to what was found with the extended Amiet's model, the finite chord has an impact below about 3000 Hz, yielding lower levels below 400 Hz and higher levels beyond that frequency with a peak difference of about 4 dB at 1500 Hz. Figure 9 (right) compares predictions from all the models

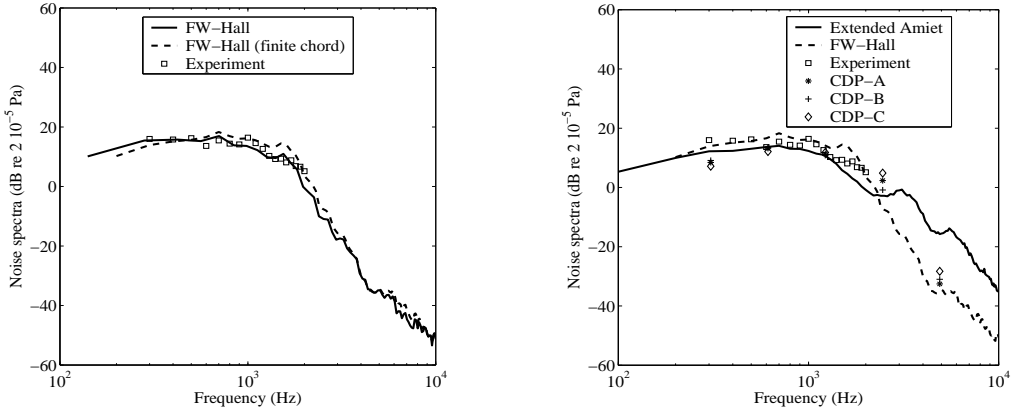


FIGURE 9. Far field acoustic spectra in the midspan plane above the airfoil ($\theta = 90^\circ$) at $R = 2$ m from the trailing edge. Left: Effect of the finite chord. Right: Comparisons of all models.

presented in Section 5.1. In the extended Amiet's prediction, the reference LES data has been used again as the spanwise coherence length is better converged (Fig. 5 (right)). Yet the faster decay observed at high frequencies in Fig. 5 (left) of the wall-pressure spectrum near the trailing edge of the reference LES causes an under-prediction of the model based on wall-pressure statistics beyond 1500 Hz. If any CDP LES wall-pressure spectrum had been used instead, this discrepancy would have been minimal. The noise calculations using the numerical Green's function given by Eq. 5.6 with \tilde{T}_{ij} from the three CDP runs have been computed at five discrete frequencies: 291, 583, 1166, 2332, and 4664 Hz. They show very similar spectral values as the prediction of Ffowcs Williams-Hall's theory and very little differences between the three different grids. The maximum difference is only 4 dB at the two higher frequencies, which correspond to the frequency range where significant discrepancies were found in the velocity spectra (Fig. 8). The exact Green's function, which for instance accounts for the airfoil camber, has the largest impact on the far field noise at lower frequencies below 1000 Hz and reduces the levels even further than the finite chord. Finally, it should be stressed that all the diffraction effects from the experimental setup need to be removed to further improve the current comparisons.

6. Conclusions

With the ultimate goal of simulating the noise of complex automotive engine cooling fan blades, LES with the recently developed unstructured-grid CDP code has been performed on three different grids, and the results are compared with those from a reference structured-grid LES. The latter was previously shown to provide reasonably accurate unsteady flow in the trailing-edge region for good noise predictions compared with the ECL wind tunnel measurements. The accuracy of all simulations are assessed by comparing with detailed pressure and velocity measurements made using flush-mounted remote microphone probes and hot-wire anemometry, respectively.

The CDP runs provide good overall wall-pressure predictions: the size of the recirculation bubble is slightly over-predicted and the levels of the fluctuations at the trailing edge are too high (up to 5 dB) at lower frequencies, but these simulations show a roll-off at high frequencies closer to experiment than the reference LES. These results suggest that

the pressure coefficient and the high frequency content of the pressure fluctuations are more dependent on the LES code and its subgrid-scale model implementation, whereas the grid seems to be more critical for the pressure spectra at lower frequencies. The coherence plots show that the spanwise coherence still requires longer run times and is not easily attainable at an affordable cost.

The CDP runs also show good mean velocity profiles in the near wake but the simulation on the fully unstructured grid (CDP-C) significantly under-predicts the dissipation in the wake. Similarly, all simulations predict the shapes of the rms velocity components and the location of the peak turbulence intensity correctly in the near wake. Yet the results from the fully unstructured grid (CDP-C) deviate noticeably from the experimental rms profiles beyond $x/c \approx 0.13$ and significantly under-predict the velocity spectra beyond 1500 Hz. This study suggests that the velocity field in the wake is very sensitive to the grid coarsening in both streamwise and cross-flow directions and that further work is needed to improve the fully unstructured grid.

The observed near-field discrepancies are shown, however, to have only a small impact on the acoustic predictions made with two different approaches, which compare favorably with the ECL anechoic wind tunnel measurements. Both the extended Amiet's theory based on the wall-pressure statistics and the Ffowcs Williams-Hall's theory based on the velocity statistics yield similar results. The impact of accounting for the finite chord length in both theories is the same, leading to discrepancies limited to frequencies below 3000 Hz and peaked at 4 dB difference around 1500 Hz. Finally, taking the exact Green's function instead of the flat plate approximation further reduces the noise levels at lower frequencies. It is shown that the increasing numerical errors in the velocity fields from the different CDP simulations can yield up to 4 dB discrepancies in sound spectra at high frequencies.

Acknowledgments

The authors would like to thank Professor John Foss of Michigan State University for his helpful discussions and support and Seongwon Kang for providing the initial CDP-A results.

REFERENCES

- AMIET, R. K. 1976 Noise due to turbulent flow past a trailing edge. *J. Sound Vib.* **47**(3), 387–393.
- CARO, S. & MOREAU, S. 2000 Aeroacoustic modeling of low pressure axial flow fans. *AIAA Paper 2000-2094*, 6th AIAA/CEAS Aeroacoustics Conference, Lahaina, Hawaii.
- FFOWCS WILLIAMS, J. E. & HALL, L. H. 1970 Aerodynamic sound generation by turbulent flow in the vicinity of a scattering half plane. *J. Fluid Mech.* **40**, 657–670.
- FUKANO, T., KODAMA, Y. & SENOO, Y. 1977 Noise generated by low pressure axial flow fans. 1 - Modelling of the turbulent noise. *J. Sound Vib.* **50**(1), 63–74.
- GERMANO, M., PIOMELLI, U., MOIN, P., AND CABOT, W. H., 1991 A dynamic subgrid-scale eddy viscosity model. *Phys. Fluids A* **3**(7), 1760–1765.
- GERSHFELD, J. 2004 Leading edge noise from thick foils in turbulent flows. *J. Acoust. Soc. Am.* **116**(3), 1416–1426.

- GLEGG, S. A. L., BAXTER, S. M. & GLENDINNING, A. G. 1987 The prediction of broadband noise from wind turbines. *J. Sound Vib.* **118**(2), 217–239.
- HAM, F. & IACCARINO, G. 2004 Energy conservation in collocated discretization schemes on unstructured meshes. *Annual Research Briefs-2004*, Center for Turbulence Research, Stanford Univ./NASA Ames.
- HOWE, M. S. 2001 Edge-source acoustic Green's function for an airfoil of arbitrary chord with application to trailing-edge noise. *The Quarterly Journal of Mechanics and Applied Mathematics* **54**(1), 139–155.
- HUBBARD, H. H. & SHEPHERD, K. P. 1991 Aeroacoustics of large wind turbines. *J. Acoust. Soc. Am.* **89**, 2495–2507.
- KIM, J. & MOIN, P. 1985 Application of a fractional-step method to incompressible Navier-Stokes equations. *J. Comput. Phys.* **59**, 308–323.
- LILLY, D. K. 1992 A proposed modification of the Germano subgrid-scale closure method. *Phys. Fluids A* **4**, 633–635.
- MAHESH, K., CONSTANTINESCU, G. & MOIN, P. 2004 A numerical method for large-eddy simulation in complex geometries. *J. Comput. Phys.* **197**, 215–240.
- MOREAU, S., HENNER, M., IACCARINO, G., WANG, M. & ROGER, M. 2003 Analysis of flow conditions in free-jet experiments for studying airfoil self-noise. *AIAA J.* **41**(10), 1895–1905.
- MOREAU, S., IACCARINO, G., KANG, S., KHALIGHI, Y. & WANG, M. 2004 Towards a large eddy simulation of a low speed fan blade. *Proceedings of the Summer Program 2004*, Center for Turbulence Research, Stanford Univ./NASA Ames.
- MOREAU, S. & ROGER, M. 2005 Effect of airfoil aerodynamic loading on trailing edge noise. *AIAA J.* **43**(1), 41–52.
- MOREAU, S., MENDONCA, F., QAZI, O., PROSSER, R. & LAURENCE, D. 2005 Influence of turbulence modeling on airfoil unsteady simulations of broadband noise sources. *AIAA Paper 2005-2916*, 11th AIAA/CEAS Aeroacoustics Conference, Monterey, California.
- MOREAU, S., NEAL, D. & FOSS, J. 2006 Hot-wire measurements around a Controlled Diffusion airfoil in an open-jet anechoic wind tunnel. *J. Fluid Engineering* **28**(4), 699–706.
- MOREAU, S., HENNER, M., CASALINO, D., GULLBRAND, J., IACCARINO, G. & WANG, M. 2006 Towards the prediction of low speed fan noise. *Proceedings of the Summer Program 2006*, Center for Turbulence Research, Stanford Univ./NASA Ames.
- PARCHEN, R., HOFFMANS, R., GORDNER, A., BRAUN, K. A., VAN DER BORG, N. J. C. & DASSEN, M. AND A.G.M. 1999 Reduction of airfoil self-noise at low Mach number with a serrated trailing edge. 6th International Congress on Sound and Vibration, Copenhagen, Denmark, 3433–3440.
- PÉRENNÈS, S. & ROGER, M. 1998 Aerodynamic noise of a two-dimensional wing with high-lift devices. *AIAA Paper 98-2338*, 4th AIAA/CEAS Aeroacoustics Conference, Toulouse, France.
- ROGER, M. & MOREAU, S. 2004 Trailing edge noise measurements and prediction for a subsonic loaded fan blade. *AIAA J.* **42**(3), 536–544.
- ROGER, M. & MOREAU, S. 2005 Back-scattering correction and further extensions of Amiet's trailing edge noise model. Part 1: theory. *J. Sound Vib.* **286**(3), 477–506.
- SHARLAND, I. J. 1964 Sources of noise in axial flow fans. *J. Sound Vib.* **1**(3), 302–322.

- SINGER, B. A., LOCKARD, D. P. & BRENTNER, K. S. 2000 Computational aeroacoustic analysis of slat trailing-edge flow. *AIAA J.* **38**(9), 1558–1564.
- STROHL, A. & COMTE-BELLOT, G. 1973 Aerodynamic effects due to configuration of X-wire anemometers. *Trans. ASME, J. Appl. Mech.* **40**, 661–666.
- ABDEL-RAHMAN, A., TROPEA, C., SLAWSON, P., AND STRONG, A. 1987 On temperature compensation in hot-wire anemometry. *J. Phys. E.: Sci Instr.*, **20**, 315–316.
- WANG, M. & MOIN, P. 2000 Computation of trailing-edge flow and noise using large-eddy simulation. *AIAA J.* **38**(12), 2201–2209.
- WANG, M., MOREAU, S., IACCARINO, G. & ROGER, M. 2004 LES prediction of wall pressure spectra on a low speed airfoil. *Annual Research Briefs-2004*, Center for Turbulence Research, Stanford Univ./NASA Ames.
- WRIGHT, S.E. 1976 The acoustic spectrum of axial flow machines. *J. Sound Vib.* **45**(2), 165–223.